Decadal variability of eddy temperature fluxes in the Labrador Sea

Christopher Danek[1,2*], Patrick Scholz[1] and Gerrit Lohmann[1,2]

[1]Alfred Wegener Institute for Polar and Marine Research (AWI), Bremerhaven, Germany
[2]MARUM-Center for Marine Environmental Sciences, Bremen, Germany

Key Points:

- Eddy temperature fluxes through baroclinic instabilities yield mixed layer restratification in the Labrador Sea deep convection zone.
- In addition, buoyant waters must be provided by the boundary current to balance the destabilizing forcing.
- At 20 km local horizontal resolution, modeled and parameterized fluxes are too weak to increase stratification as seen in the 5 km case.

*Alfred Wegener Institute for Polar and Marine Research, Am Handelshafen 12, 27570 Bremerhaven, Germany

Corresponding author: Christopher Danek, cdanek@awi.de

Abstract

Oceanic mesoscale eddies play an important role in preconditioning and restratifying the water column before and after mixing events, thereby affecting deep water formation variability. In the Labrador Sea, where deep convection occurs regularly, observations and models indicate a complex interplay of turbulence and associated tracer fluxes. Results from a realistic eddy-resolving ($\sim$5 km local horizontal resolution) ocean model in quasi-equilibrium ($\sim$300 years integration) suggest that small-scale temperature fluxes due to turbulent potential to kinetic energy conversion are the main driver of mixed layer restratification during deep convection triggered through atmospheric forcing. In addition to these baroclinic instabilities, buoyant water masses must be provided by the boundary current, where barotropic turbulence is equally important. Only acting together, the destabilizing forcing can be balanced. In a low-resolution control simulation ($\sim$20 km) the modeled turbulence is strongly reduced and the associated modeled and parameterized heat fluxes too weak to increase stratification.

Plain Language Summary

The ocean circulation includes many swirls. These ”eddies” are only a few tens km wide and transport temperature and salt, both of which change the density of the water and hence the circulation itself. Since these eddies are so small, they are not incluced in climate models and their effects must be added by parameterizations. Here we use a global ocean model with a locally refined resolution so that eddies are directly modeled. We see that the influence of the eddies is very large, especially in restoring the stability of the water column after deep convection events. Different turbulent instability processes are the reason why eddies evolve. In a coarser model resolution, however, we find that the parameterization of the eddy effects is too weak.

1 Introduction

Eddies are ubiquitous in the world ocean, particularly in vicinity of strong currents, e.g. the Gulf Stream or North Atlantic Current (Chelton et al., 2011). On length scales of the local baroclinic Rossby radius of deformation these vortices yield mesoscale temperature and freshwater fluxes which modify sea water properties and thereby change the ocean circulation. Similarly, biogeochemical nutrient fluxes such as chlorophyll concentrations are altered, affecting phytoplankton and biomass production (Danabasoglu et al., 1994; Z. Zhang et al., 2014; Fröb et al., 2016).

The Labrador Sea (LS) basin is a region of frequent deep convection during winter time, and thereby an important place of deep water formation (Rhein et al., 2015). Here, eddies were observed to contribute to preconditioning before and restratification after mixing events (e.g. Marshall & Schott, 1999; Lilly et al., 2003; Straneo, 2006; Palter et al., 2008; de Jong et al., 2014; Rykova et al., 2015; Yashayaev & Loder, 2016; W. Zhang & Yan, 2018). However, the exact route of turbulence remains unclear due to sparsity of available observations. Numerical model experiments suggest a complex interplay of barotropic and baroclinic instabilities as the source of eddy kinetic energy (EKE) and associated mesoscale tracer fluxes. During winter, Irminger Rings (IR) separate from the West Greenland Current (WGC), eventually providing buoyant waters for the weakly stratified LS interior. Additionally, convective eddies in the vicinity of the deep convection patch work to flatten steep isopycnals. However, due to complex geometry of the LS basin and high computational costs of high-resolution models, experiments with a realistic eddy resolving setup are rather short and focus on the mean state or the mean annual cycle (Chanut et al., 2008; McGeehan & Maslowski, 2011; Kawasaki & Hasumi, 2014; Saenko et al., 2014; W. Zhang & Yan, 2014; Dukhovskoy et al., 2016; Rieck et al., 2019).

In this study we use the global ocean model FESOM (Wang et al., 2014) with a locally mesoscale-resolving horizontal resolution of $\sim$5 km and provide a coherent picture of turbulence and associated mesoscale temperature fluxes. We integrated the model for 310 years, to examine a decadal time-scale perspective of the complex LS mixed layer restratification dynamics. In addition, a low-resolution ($\sim$20 km local horizontal resolution) setup serves as control run to investigate the influence of the model resolution.

2 Methods

2.1 Ocean Model FESOM

We utilized the global Finite Element Sea ice–Ocean Model (FESOM) version 1.4 (Wang et al., 2014). To analyze the resolution-dependence of the involved dynamical processes during MLD restratification, low- and high-resolution FESOM grids were designed.

The details of the model grids and set ups are described in Danek et al. (2019) and are shown in the supplement (Text S1 and Fig. S1).

2.2 Eddy Temperature Fluxes and Eeddy Kinetic Energy

The Boussinesq tendency equation for depth-integrated temperature T in flux form (in °C m s^{-1}) can be written as

$$\partial_t \int_z T \, \mathrm{d}z = - \int_z \boldsymbol{\nabla} \cdot (\mathbf{u} + \mathbf{u}_{\mathrm{SGS}}) T \, \mathrm{d}z + F + \mathrm{Rest} \tag{1}$$

with ∂_t being the partial derivative with respect to time, $\boldsymbol{\nabla}$, $\mathbf{u}$ and $\mathbf{u}_{\mathrm{SGS}}$ the three-dimensional spatial derivative, velocity and sub-grid scale (SGS) velocity vectors, with the latter arising from the Redi and GM parameterizations (Redi, 1982; Gent & McWilliams, 1990). The first term on the right hand side represents the temperature advection divergence. As any vector transport may be separated (Helmholtz theorem) in a divergent and a rotational component, $\mathbf{u}T = (\mathbf{u}T)_{\mathrm{D}} + (\mathbf{u}T)_{\mathrm{R}}$ (e.g., Zdunkowski & Bott, 2003), using the flux form here is advantageous since the rotational part of the vector field does not affect the dynamics of the flow (Marshall & Shutts, 1981; Jayne & Marotzke, 2002; Fox-Kemper et al., 2003), and, by definition, the rotational part is divergence-free ($\boldsymbol{\nabla} \cdot (\mathbf{u}T)_{\mathrm{R}} = 0$). The thermodynamic boundary condition at the sea surface $F = (\rho \, c_{\mathrm{p}})^{-1} Q_{\mathrm{net}}$ uses the sea surface density ρ and the specific heat capacity of sea water at constant pressure c_{p} as well as the calculation of the net surface heat flux Q_{net} through the CORE-II forcing (Large & Yeager, 2009). All other components are subsumed in the Rest term (e.g. diffusion and non-local transports through the KPP vertical mixing scheme of Large et al., 1994).

To distinguish between temperature fluxes from long and short time scales, Reynolds averaging (e.g., Vallis, 2017) of the horizontal advection term yields

$$-\boldsymbol{\nabla}_{\mathrm{h}} \cdot (\mathbf{u}_{\mathrm{h}} + \mathbf{u}_{\mathrm{SGS,h}}) T = -\boldsymbol{\nabla}_{\mathrm{h}} \cdot \left(\overline{\mathbf{u}}_{\mathrm{h}} \overline{T} + \overline{\mathbf{u}_{\mathrm{h}}' T'} + \overline{\mathbf{u}_{\mathrm{SGS,h}} T} \right), \tag{2}$$

where the subscript h indicates the horizontal component of a vector, the overbar a temporal mean and the prime a deviation from that mean. Following von Storch et al. (2012), we derive the eddy temperature flux $\overline{\mathbf{u}'T'} = \overline{\mathbf{u}T} - \overline{\mathbf{u}}\overline{T}$ by calculating the total temperature flux $\mathbf{u}T$ in every model time step and save its monthly mean $\overline{\mathbf{u}T}$. As such, $\overline{\mathbf{u}'T'}$ represents deviations on temporal scales from the model time step to a month without the necessity of saving large high-resolution 3D model data on a high temporal frequency.

Fig. S2 confirms that similar monthly mean eddy fluxes are obtained with this method, independent of the model output frequency choice.

To identify the sources and sinks of the eddy kinetic energy (EKE) $\mathbf{u}_\mathrm{h}'^2/2$ (neglecting vertical velocity w due to hydrostatic approximation), the Lorenz Energy Cycle (Lorenz, 1955) can be applied (Böning & Budich, 1992; Marchesiello et al., 2003; von Storch et al., 2012; Renault et al., 2016). The volume-integrated EKE tendency equation, derived from the hydrostatic Boussinesq momentum balance (Olbers et al., 2012),

$$\partial_t \int_V \mathrm{EKE}\,\mathrm{d}V = \int_A (F_e K_e + \text{bottom stress})\,\mathrm{d}A + \int_V (\mathrm{HRS} + \mathrm{VRS} + P_e K_e + \epsilon)\,\mathrm{d}V\,, \quad (3)$$

yields the individual energy conversion terms which change EKE during instability processes and associated interactions with the mean flow (in m^5 s^{-3}; signs do not represent physical direction). $F_e K_e = {\rho_0}^{-1}\,(\overline{\mathbf{u}_\mathrm{h}' \cdot \boldsymbol{\tau}'})$ represents eddy growth through work of wind anomalies at the sea surface via wind stress $\boldsymbol{\tau}$ (in kg m^{-1} s^{-2}) and can be understood as a mechanical source of instability (vice versa, friction at the bottom leads to EKE removal). The horizontal and vertical Reynolds stresses $\mathrm{HRS} = -\overline{u'^2}\,\partial_x \overline{u} - \overline{u'v'}\,\partial_y \overline{u} - \overline{u'v'}\,\partial_x \overline{v} - \overline{v'^2}\,\partial_y \overline{v}$ and $\mathrm{VRS} = -\overline{u'w'}\,\partial_z \overline{u} - \overline{v'w'}\,\partial_z \overline{v}$ yield EKE from barotropic instabilities of the mean flow due to horizontal and vertical shear. As such, VRS represents Kelvin-Helmholtz instability. Their sum is the barotropic transfer from mean to eddy kinetic energy $K_m K_e = \mathrm{HRS} + \mathrm{VRS}$. $P_e K_e = \overline{w'b'}$ with buoyancy $b = -g{\rho_0}^{-1}\,\rho$ is associated with baroclinic instability through the exchange between turbulent potential and kinetic energy. ϵ represents dissipation of EKE by small-scale turbulence implemented in the model via viscosity. These energy conversions are defined such that if positive, EKE is generated at the expense of the mean flow. In turn, if negative, EKE is transferred back to the mean flow (or dissipated) by turbulence.

3 Results

3.1 Temperature Flux Divergence

On average (1948-2009, the whole forcing period), the Labrador Sea (LS) looses heat to the atmosphere through outgoing longwave radiation and sensible and latent heat fluxes ($F < 0$; Fig. 1a,b). The average horizontal surface circulation is characterized by the quiescent LS interior surrounded by the fast (>25 cm s^{-1}) West Greenland Current (WGC) along the southwest coast of Greenland in northwestward direction and further downstream along the eastern coast of Canada as the Labrador Current (LC) in southeastward direction (arrows in Fig. 1a,b). The boundary current in the high-resolution model (∼5 km local horizontal resolution) is narrower and faster compared to the low-resolution control run (∼20 km local horizontal resolution). The transition between the WGC and LC is separated into two main branches in the high-resolution run, while being one broad structure in the low-resolution model. Similarly, vertical velocities are much faster in the high-resolution LS (not shown). The average low-resolution March mixed layer depth (MLD) extends to a large area deeper than ∼2 km while being confined to a small part of the ∼3 km depth area in the high-resolution run (white contours show the 1.5 and 2 km MLD). Here, MLD is defined as the depth at which the potential density σ_θ deviates from its 10 m depth value by 0.125 kg m^{-3} (Danabasoglu et al., 2014).

The average depth-integrated mean horizontal temperature advection divergence covers a broad range between 10^{-4} to 10^{-1} °C m s^{-1} with the largest values along the WGC between the 2 and 3 km isobaths (black lines in Fig. 1c,d: positive values indicate a temperature gain). In both model runs, the boundary current advects temperature away from the coast towards the interior. This process is stronger and more confined in the high-resolution run, similarly as the circulation pattern. In the LS interior, the mean temperature advection is ∼1 order of magnitude smaller compared to the boundary currents. Here, divergent and convergent patches coexist next to each other. This feature is much more heterogeneous in the high-resolution model with a large number of divergent and convergent patches on spatial scales of a few hundreds of km.

The average depth-integrated eddy (i.e. fluctuations on temporal scales from the model time step to a month) temperature advection divergence is generally smaller by ∼1 order of magnitude compared to the mean component with largest values along the WGC and LC in both model setups (Fig. 1e,f). In the broad low-resolution WGC, temperature decreases by eddy advection in the region confined to the 2 and 3 km isobaths and increases on- and offshore of this patch. This feature of enhanced eddy temperature divergence/convergence is spatially limited to the WGC and weakens in magnitude directly after separation from the coast at ∼53°W. In the LC, the low-resolution eddy fluxes feature a similar dipole pattern as the mean component with convergence in the region bounded by the 1-2 km isobaths and temperature loss in the region of 2-3 km depth. Hence, mean and eddy components are of opposite sign in these areas (Fig. 1 c,e). In the LS interior, similarly as for the mean, patches of convergent and divergent eddy temperature fluxes coexist in both the low- and high-resolution models with the latter being much more dynamic on small spatial scales. In addition, enhanced eddy fluxes in the WGC persist long after the separation from the Greenland coast towards $\sim$56°W (Fig. 1f). In contrast to the low-resolution run, mean and eddy components along the WGC and LC are of the same sign, especially along the 2 km isobath (Fig. 1d,f). The high-resolution run exhibits a second branch of enhanced eddy temperature divergences downstream the WGC at $\sim$64°N, which is absent in the low-resolution control.

In the LS interior, atmospheric forcing triggers deep convection events throughout the observational period (Fig. 2a). During positive NAO years (years with positive phase of the North Atlantic Oscillation; Hurrel, 2003), an increased oceanic heat loss to the atmosphere yields deep winter MLDs of several km depth in March (month with the deepest MLD on average in both model runs, not shown). The decadal MLD evolution reveals pronounced differences between the low- and high-resolution models. While the high-resolution MLD is in phase with the NAO, the low-resolution model exhibits almost no temporal variability and remains at deep MLDs throughout the forcing period (Fig. 2a). A similar picture emerges for the horizontal eddy temperature advection divergence, volume-integrated over the respective MLD within the LS interior (index area shown in Fig. 1a,b). While the large-scale circulation poses a temperature loss in the convection zone, high-resolution eddy fluxes temporarily become active and reduce or even balance this heat loss during deep convection events (Fig. 2c). These dynamics are almost absent in the low-resolution model, where the eddy contribution is much weaker and hardly balances the heat loss due to the mean circulation (Fig. 2b). Here, SGS fluxes are strongly enhanced compared to the near-zero values of the high-resolution model (red dashed lines in Fig. 2b,c). However, the total temperature advection divergence including the SGS contribution stays negative throughout the forcing period in the low-resolution run.

3.2 EKE Generation

During March, EKE is generated through turbulent wind work $F_e K_e$ at the sea surface with enhanced values in ice-free regions (Fig. 3a,b). Depth-integrated barotropic HRS leads to eddy growth on the expanse of the mean flow on the offshore side of the WGC, before and after separation from the Greenland coast (Fig. 3c,d). In a narrow patch between the 1 and 2 km isobaths along the coasts of Greenland and Canada, eddies transfer energy back the mean flow by horizontal shear (HRS < 0). The high-resolution run exhibits much larger values of this barotropic instability compared to the low-resolution setup. These large HRS values drop by ∼2 orders of magnitude towards the LS interior. Depth-integrated baroclinic instability P_eK_e is responsible for an EKE increase almost everywhere in the LS basin (Fig. 3e,f). Its general pattern resembles the barotropic one with enhanced values along the WGC and the downstream circulation. The region of large depth-integrated HRS and P_eK_e corresponds with the depth-integrated EKE which is a multiple in the high- compared to the low-resolution run. Here, this area also marks the approximate edge of the average March MLD patch (thick white contours in Fig. 3d,f and b, respectively).

The wind forcing poses a constant source of EKE with decadal fluctuations of similar magnitude as the average seasonal cycle (strongest during winter; Fig. S3a). Area-integrated over the LS interior, both models exhibit similar F_eK_e values with small differences probably arising from faster surface currents in the high-resolution run (solid lines in Fig. 4a; left axis). Volume-integrated barotropic and baroclinic EKE conversion terms, in contrast, differ greatly between low- and high-resolution runs (solid lines in Fig. 4b,c; left axes). During deep convection events in the early 1970s, mid-1980s and early to mid-1990s, high-resolution barotropic and baroclinic instabilities are strongly enhanced in the LS interior. Negative HRS and VRS (much weaker; dashed lines in Fig. 4b; right axis) lead to a removal of EKE in the LS interior. However, baroclinic instabilities P_eK_e let eddies grow within the LS interior with an efficiency of one order of magnitude larger than the combined barotropic instabilitites K_mK_e. Hence, the evolution of the volume-integrated EKE closely follows P_eK_e (dashed lines in Fig. 4c; right axis). Similar proportions apply, although much reduced in absolute numbers, to the low-resolution run and to the average seasonal cycle (Fig. S3b-e). Throughout the forcing period, the EKE contribution to the total kinetic energy $\mathbf{u}_\mathrm{h}{}^2/2$ does not show those pronounced peaks during deep water formation events but stays rather around 25% in the low- and around 45% in the high-resolution run (dashed lines in Fig. 4a; right axis). Their decadal fluctuations are of similar magnitude as the average seasonal cycle (largest during winter; Fig. S3f).

4 Discussion

At a local horizontal resolution of ∼5 km our high-resolution FESOM setup exhibits turbulent temperature fluxes of baroclinic origin which lead to an efficient MLD restratification in the LS interior. At a slightly decreased local resolution of ∼20 km, these fluxes are too weak to increase stability (parameterized SGS fluxes taken into account). Our results support the view that meso- to submesoscale baroclinic mixed layer instabilities are essential for restratifying the water column after convection. Baroclinic instability induced through large ageostrophic velocities (Lavender et al., 2002) draws turbulent potential energy from steep isopycnals, which thereby flatten (Fox-Kemper et al., 2008).

However, generating enough EKE within the convergence zone is only half of the story. As seen in other high-resolution ocean modeling results, the temperature flux divergence is enhanced along the fast boundary current (Chanut et al., 2008; Kawasaki & Hasumi, 2014; Saenko et al., 2014; de Jong et al., 2016). In addition, observations indicate that eddies generated within and advected with the boundary current transport heat and salt (or freshwater) into the LS interior (Irminger Rings; Jones & Marshall, 1997; Lilly et al., 2003; Straneo, 2006; Schmidt & Send, 2007; Rykova et al., 2009; de Jong et al., 2014; Rykova et al., 2015). This implies that the seawater properties of the boundary current set the restratification ability of the eddies, also reflected by large HRS in the WGC in our high-resolution run. The efficient MLD restratification seen in our high-resolution FESOM setup was only achieved when the boundary current was not biased too dense and thus being able to provide buoyant water masses (i.e. after some adjustment forcing cycles; Danek et al., 2019). Hence, if no buoyant water is available in the interior, convective eddies induced through baroclinic instabilities may not contribute to restratification. This view is supported by model results where a suppressed turbulence in the WGC led to an underestimation of transports of heat into the LS interior by Irminger Rings and a deeper MLD (Gelderloos et al., 2011; Kawasaki & Hasumi, 2014; Rieck et al., 2019).

From the model perspective, our results imply several challenges. The energy budget reveals an important role of EKE dissipation through bottom friction and turbulence implemented via viscosity. Physical dissipation, however, was shown to be strongly affected by spurious unphysical numerical dissipation on meso- to submesoscales in ocean models (Soufflet et al., 2016). In addition, the vertical mixing scheme was shown to significantly change water mass properties, especially the KPP non-local flux (Griffies et al., 2015). A systematic analysis of different mixing parameterizations is missing so far. Moreover, utilizing an ocean-only model configuration excludes important feedbacks between the ocean and the atmosphere. For example, a decreased storm activity as expected through global warming leads to a decreased sea surface heat loss and drastically reduced formation rates of water masses associated with deep convection in the LS (Garcia-Quintana et al., 2019).

5 Conclusions

We provide a comprehensive picture of the LS mixed layer variability, the associated instability processes and resulting eddy heat fluxes, including, for the first time, a decadal time-scale perspective. On ∼5 km local resolution, mixed layer restratification is accomplished through baroclinic instabilities in the convective patch as well as the advection of buoyant waters from the boundary current by turbulent fluxes induced through horizontal shear. On ∼20 km local resolution, these dynamics are not well represented and common eddy parameterizations are too weak. We conclude that high-resolution ocean model studies should examine 1) the role of both lateral and vertical mixing parameterizations and 2) if the proposed mechanisms also apply in coupled model setups with ocean-atmosphere feedbacks.

As a logical next step, we will apply our analysis in a coupled atmosphere-ocean-sea ice framework using the ocean multi-scale approach as proposed here (e.g. Sidorenko et al., 2019; Lohmann et al., 2020). Past climates provide a possibility to evaluate the performance of general circulation models. Key findings are that the models do not capture the magnitude of the sea surface temperature anomalies derived from data (Lohmann et al., 2013) and that they systematically underestimate the variability (Laepple & Huybers, 2014). It might be that the question of underestimated climate variability is related to our finding that the variability in key regions such as the Labrador Sea cannot be well represented and parameterizations have difficulties to provide the underlying ocean dynamics.

Acknowledgments

This work was funded through the MARUM excellence cluster “The Ocean Floor – Earth’s Uncharted Interface” and the AWI through the Helmholtz programme “Changing Earth – Sustaining our Future”. This paper is a contribution to the S2 project (Improved Parameterizations and Numerics in Climate Models) of the Collaborative Research Centre TRR 181 “Energy Transfer in Atmosphere and Ocean” funded by the Deutsche Forschungsgemeinschaft (DFG, German Research Foundation) - Projektnummer 274762653. We thank Sergey Danilov and Qiang Wang for providing the model code of FESOM1.4. The model

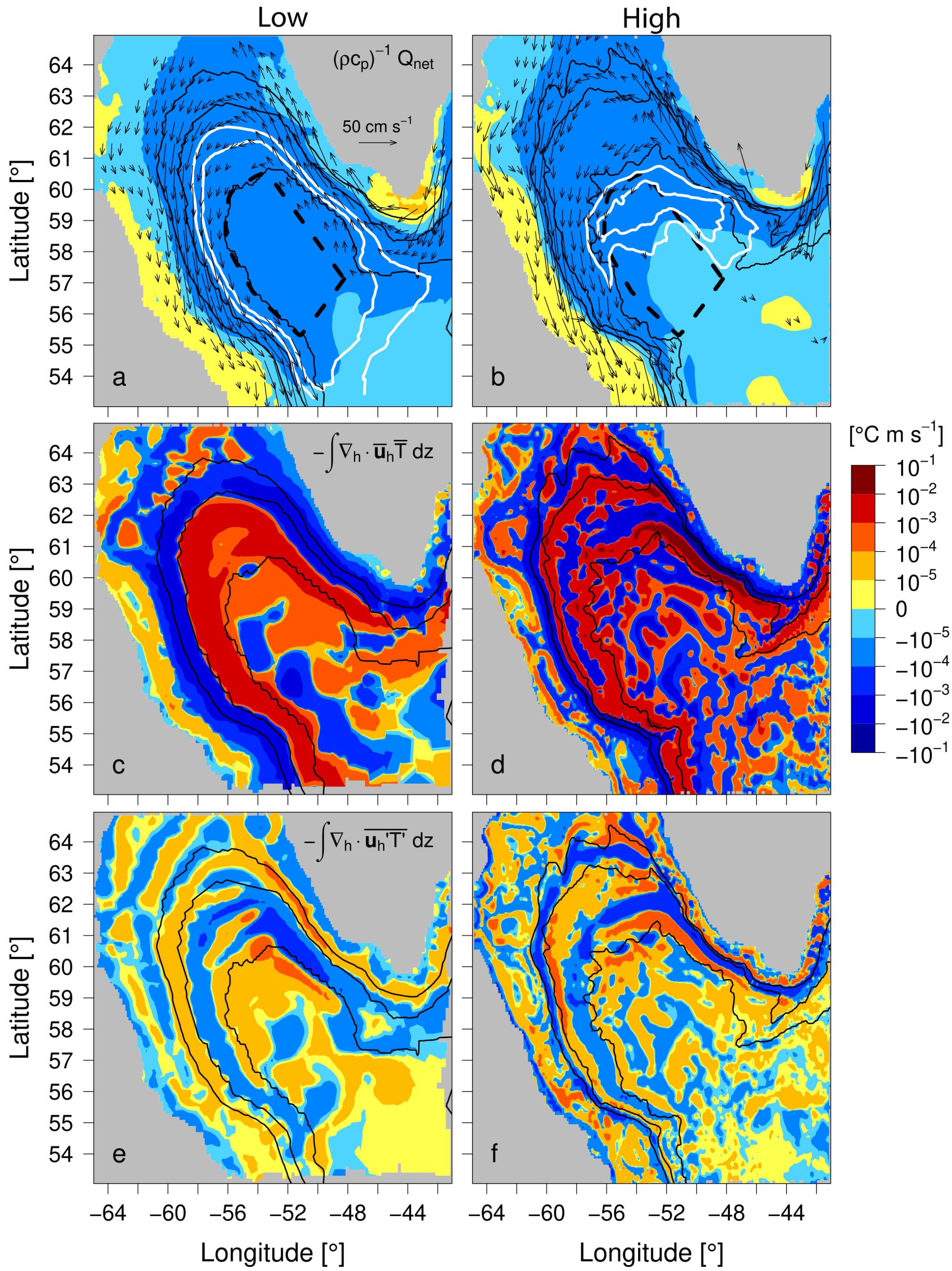

Figure 1. Average (1948-2009) local temperature changes for low- (left) and high-resolution (right) FESOM setups in the Labrador Sea. a,b) Surface flux $(\rho c_\mathrm{p})^{-1}Q_\mathrm{net}$, c,d) mean $-\nabla_\mathrm{h} \cdot \overline{\mathbf{u}}_\mathrm{h}\overline{T}$, and e,f) eddy $-\nabla_\mathrm{h} \cdot \overline{\mathbf{u}_\mathrm{h}'T'}$ depth-integrated horizontal temperature advection divergence (positive values indicate temperature gain). In a,b), arrows show direction and magnitude of the average sea surface velocity greater or equal 5 cm s^{-1}, white contours the average March 1.5 and 2 km MLD (σ_θ criterium 0.125 kg m^{-3}) and dashed thick black lines the LS interior index region. In a)-f), black contours show the 1, 2 and 3 km isobaths.

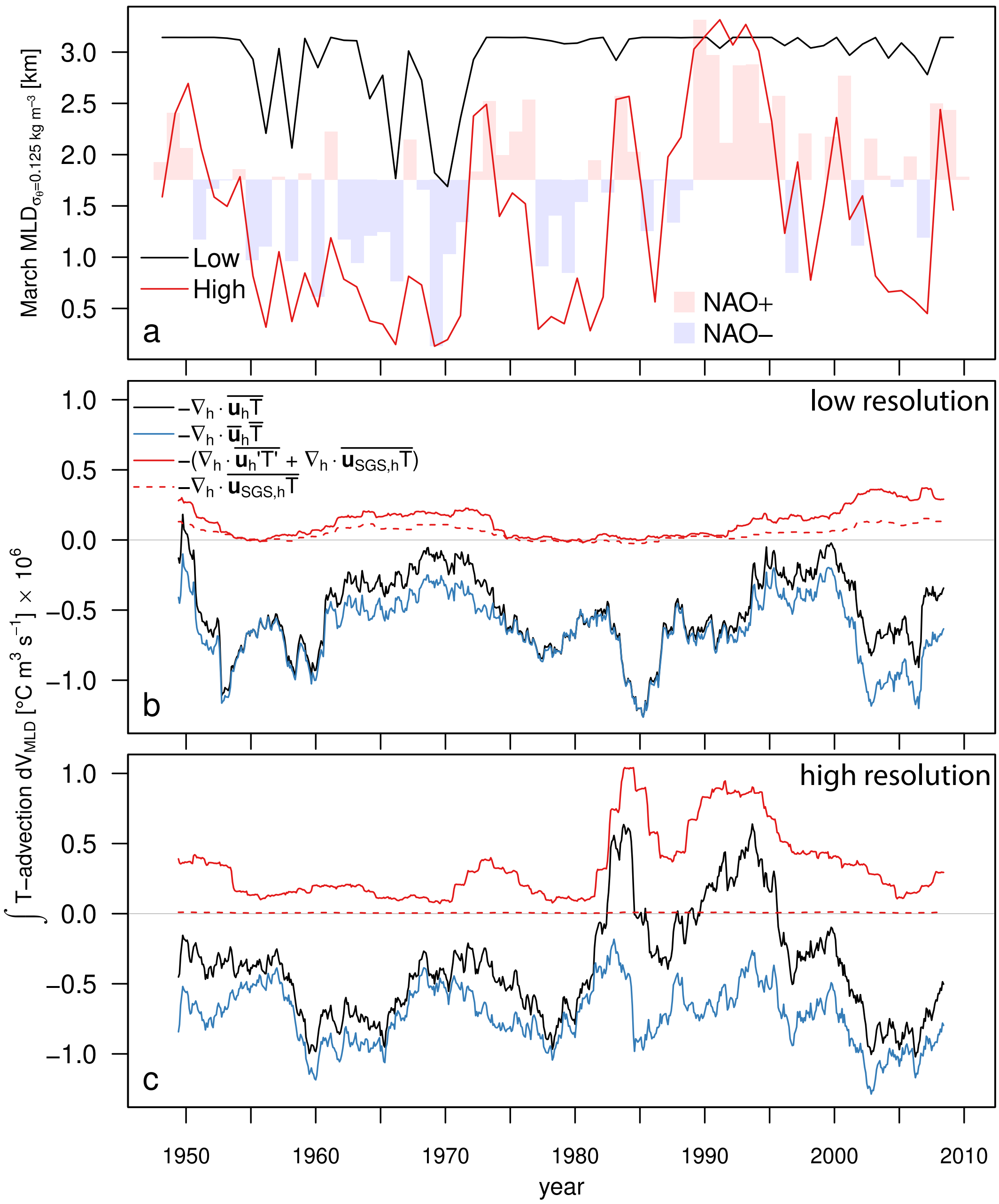

Figure 2. a) March MLD of low- (black) and high-resolution (red) FESOM setups (in km; σ_θ criterium 0.125 kg m^{-3}). Red (blue) bars in background indicate years with a positive (negative) PC-based NAO index (Hurrel, 2003). b) and c) Low- and high-resolution total horizontal temperature advection divergence $-\nabla_h \cdot \overline{\mathbf{u}_h T}$ (black lines) integrated over the LS interior (index area shown in Fig. 1a,b) from the surface to the mixed layer (positive values indicate temperature gain). Components: mean $-\nabla_h \cdot \overline{\mathbf{u}}_h \overline{T}$ (blue), combined eddy and SGS $-(\nabla_h \cdot \overline{\mathbf{u}_h' T'} + \nabla_h \cdot \overline{\mathbf{u}_{SGS,h} T})$ (red), SGS $-\nabla_h \cdot \overline{\mathbf{u}_{SGS,h} T}$ (red dashed). A 3-year running mean is applied to all advection divergence time series.

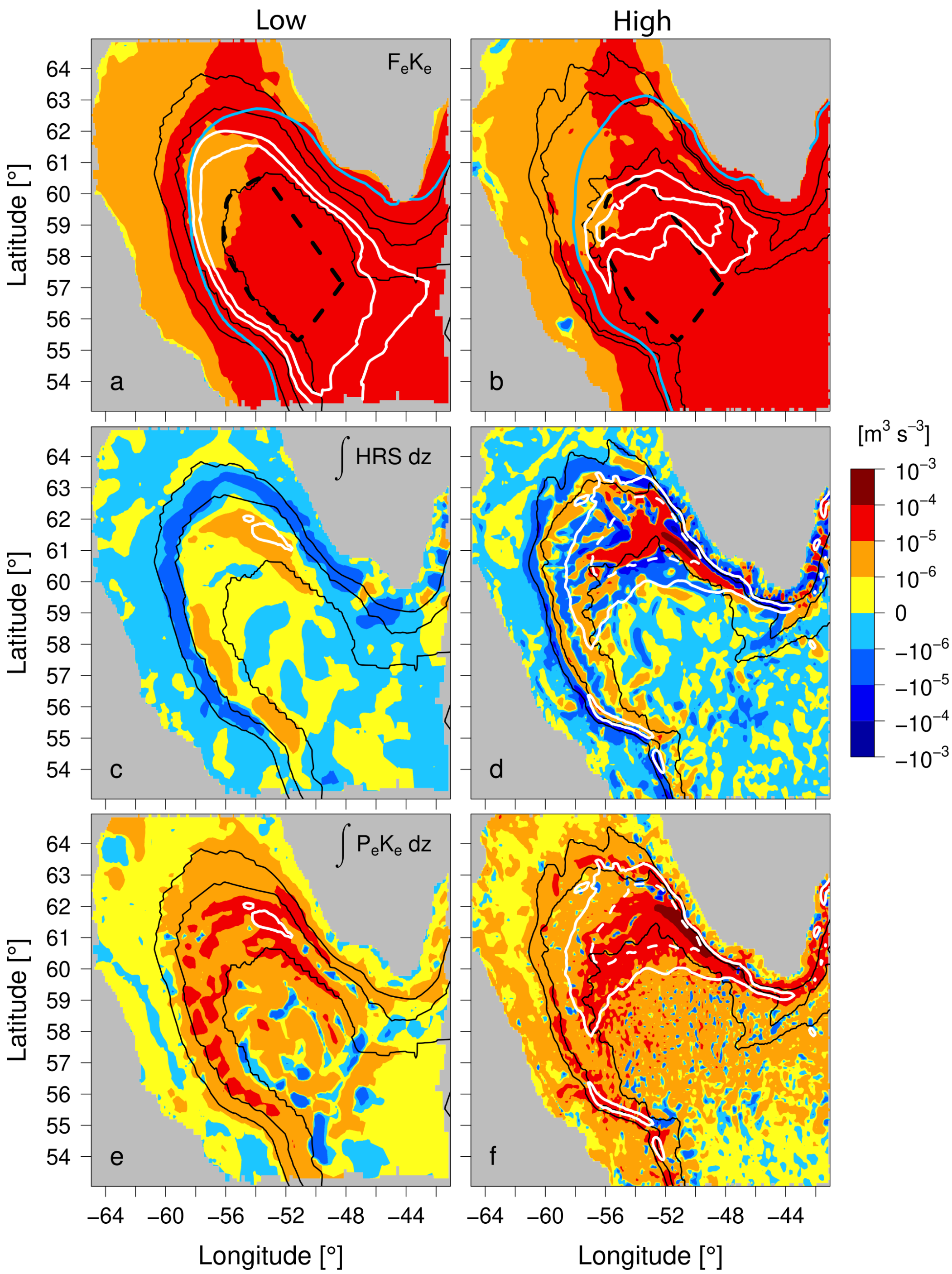

Figure 3. Average (1948-2009, March) local EKE changes low- (left) and high-resolution (right) FESOM setups in the Labrador Sea. a,b) Eddy wind work at the sea surface F_eK_e. White contours show 1.5 and 2 km MLD (σ_θ criterium 0.125 kg m^{-3}), blue contours the 15% sea ice concentration (both March mean) and dashed thick black lines the LS interior index region. c,d) Horizontal barotropic HRS and e,f) baroclinic P_eK_e depth-integrated instabilities (positive values indicate EKE generation). In c-f), white solid and dashed contours show the 5 and 20 m^3 s^{-2} depth-integrated EKE. In a)-f), black contours show the 1, 2 and 3 km isobaths.

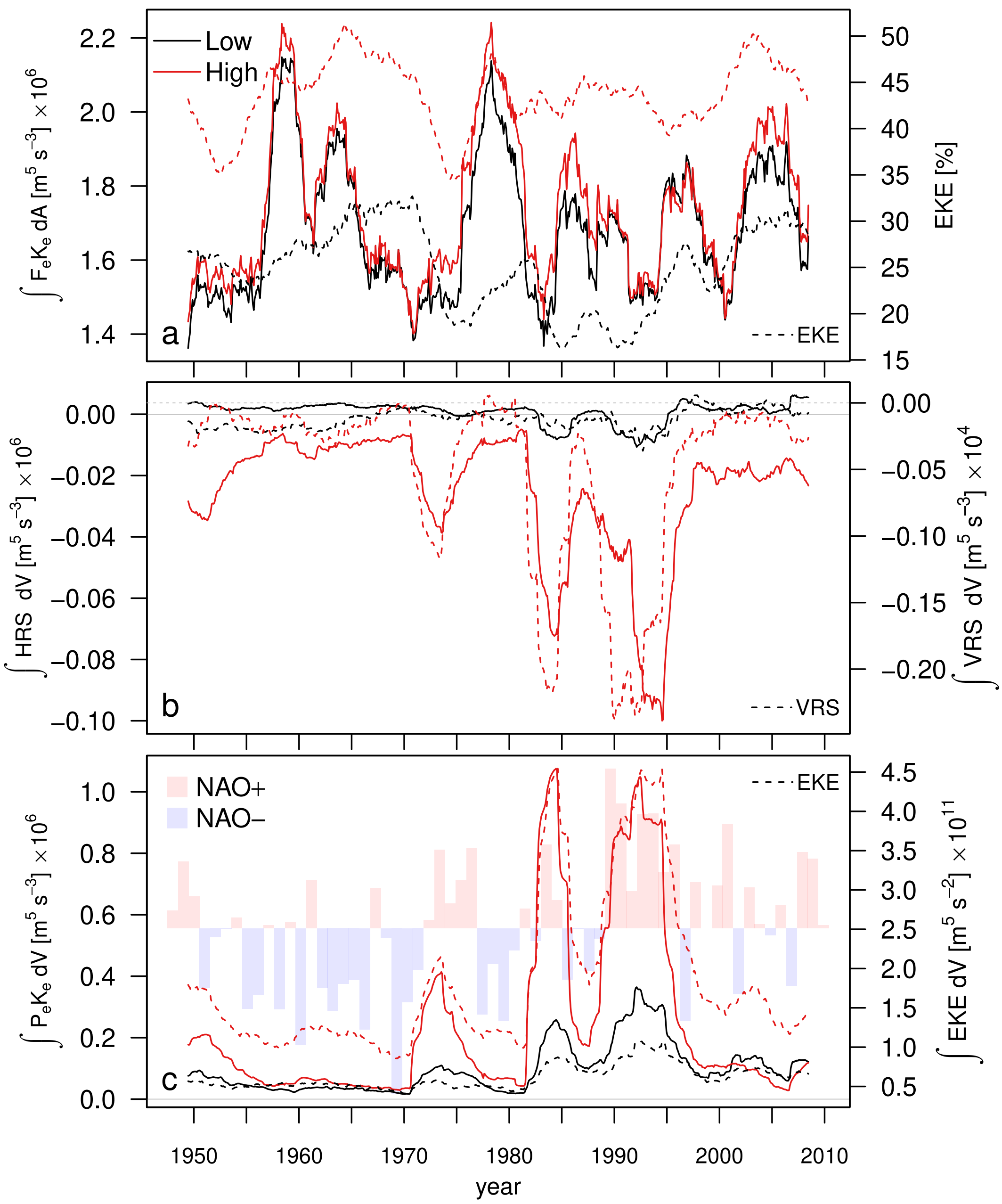

Figure 4. Decadal evolution of low- (black) and high-resolution (red) EKE changes due to a) area-integrated eddy wind work at the sea surface F_eK_e, b) horizontal barotropic HRS and c) baroclinic P_eK_e volume-integrated instabilities in the LS interior (index area shown in Fig. 1 a,b; left axes; positive values indicate an EKE generation). Dashed lines (right axes) show EKE contribution to total kinetic energy (in %; a), volume-integrated vertical barotropic instabilitites VRS (two orders of magnitude smaller than the other EKE conversions; b) and EKE (c). A 3-year running mean is applied to all time series. In c), red (blue) bars in background indicate years with a positive (negative) PC-based NAO index (Hurrel, 2003).

code used in this study and key model data that form the figures 1-4 are available at `https://doi.org/10.5281/zenodo.4896196`. We thank for the helpful and friendly support of the DKRZ (Deutsches Klimarechenzentrum) computing center. Satellite altimetry products were processed by SSALTO/DUACS and distributed by AVISO+ (`https://www.aviso.altimetry.fr`) with support from CNES.

References

Böning, C. W., & Budich, R. G. (1992). Eddy Dynamics in a Primitive Equation Model: Sensitivity to Horizontal Resolution and Friction. *Journal of Physical Oceanography*, *22*(4), 361–381. doi: 10.1175/1520-0485(1992)022<0361:ediape>2.0.co;2

Chanut, J., Barnier, B., Large, W., Debreu, L., Penduff, T., Molines, J. M., & Mathiot, P. (2008). Mesoscale Eddies in the Labrador Sea and Their Contribution to Convection and Restratification. *Journal of Physical Oceanography*, *38*(8), 1617-1643. doi: 10.1175/2008JPO3485.1

Chelton, D. B., Schlax, M. G., & Samelson, R. M. (2011). Global observations of nonlinear mesoscale eddies. *Progress in Oceanography*, *91*(2), 167-216. doi: 10.1016/j.pocean.2011.01.002

Danabasoglu, G., McWilliams, J. C., & Gent, P. R. (1994). The Role of Mesoscale Tracer Transports in the Global Ocean Circulation. *Science*, *264*(5162), 1123–1126. doi: 10.1126/science.264.5162.1123

Danabasoglu, G., Yeager, S. G., Bailey, D., Behrens, E., Bentsen, M., Bi, D., … Wang, Q. (2014). North Atlantic simulations in Coordinated Ocean-ice Reference Experiments phase II (CORE-II). Part I: Mean states. *Ocean Modelling*, *73*, 76-107. doi: 10.1016/j.ocemod.2013.10.005

Danek, C., Scholz, P., & Lohmann, G. (2019). Effects of High Resolution and Spinup Time on Modeled North Atlantic Circulation. *Journal of Physical Oceanography*, *49*(5), 1159-1181. doi: 10.1175/JPO-D-18-0141.1

de Jong, M. F., Bower, A. S., & Furey, H. H. (2014). Two Years of Observations of Warm-Core Anticyclones in the Labrador Sea and Their Seasonal Cycle in Heat and Salt Stratification. *Journal of Physical Oceanography*, *44*(2), 427-444. doi: 10.1175/JPO-D-13-070.1

de Jong, M. F., Bower, A. S., & Furey, H. H. (2016). Seasonal and Interannual

Variations of Irminger Ring Formation and Boundary–Interior Heat Exchange in FLAME. *Journal of Physical Oceanography*, *46*(6), 1717-1734. doi: 10.1175/JPO-D-15-0124.1

Dukhovskoy, D. S., Myers, P. G., Platov, G., Timmermans, M.-L., Curry, B., Proshutinsky, A., … Somavilla, R. (2016). Greenland freshwater pathways in the sub-Arctic Seas from model experiments with passive tracers. *Journal of Geophysical Research: Oceans*, *121*(1), 877-907. doi: 10.1002/2015JC011290

Fox-Kemper, B., Ferrari, R., & Hallberg, R. (2008). Parameterization of Mixed Layer Eddies. Part I: Theory and Diagnosis. *Journal of Physical Oceanography*, *38*(6), 1145-1165. doi: 10.1175/2007JPO3792.1

Fox-Kemper, B., Ferrari, R., & Pedlosky, J. (2003). On the Indeterminacy of Rotational and Divergent Eddy Fluxes. *Journal of Physical Oceanography*, *33*(2), 478-483. doi: 10.1175/1520-0485(2003)033<0478:OTIORA>2.0.CO;2

Fröb, F., Olsen, A., Våge, K., Moore, G. W. K., Yashayaev, I., Jeansson, E., & Rajasakaren, B. (2016). Irminger Sea deep convection injects oxygen and anthropogenic carbon to the ocean interior. *Nature Communications*, *7*(13244). doi: 10.1038/ncomms13244

Garcia-Quintana, Y., Courtois, P., Hu, X., Pennelly, C., Kieke, D., & Myers, P. G. (2019). Sensitivity of Labrador Sea Water Formation to Changes in Model Resolution, Atmospheric Forcing, and Freshwater Input. *Journal of Geophysical Research: Oceans*, *124*(3), 2126-2152. doi: 10.1029/2018JC014459

Gelderloos, R., Katsman, C. A., & Drijfhout, S. S. (2011). Assessing the Roles of Three Eddy Types in Restratifying the Labrador Sea after Deep Convection. *Journal of Physical Oceanography*, *41*(11), 2102-2119. doi: 10.1175/JPO-D-11-054.1

Gent, P. R., & McWilliams, J. C. (1990). Isopycnal Mixing in Ocean Circulation Models. *Journal of Physical Oceanography*, *20*(1), 150-155. doi: 10.1175/1520-0485(1990)020<0150:IMIOCM>2.0.CO;2

Griffies, S. M., Winton, M., Anderson, W. G., Benson, R., Delworth, T. L., Dufour, C. O., … Zhang, R. (2015). Impacts on Ocean Heat from Transient Mesoscale Eddies in a Hierarchy of Climate Models. *Journal of Climate*, *28*(3), 952-977. doi: 10.1175/JCLI-D-14-00353.1

Hurrel. (2003). *NAO Index Data provided by the Climate Analysis Section,* *NCAR, Boulder, USA.* (Updated regularly. Accessed 22 April 2021 at `https://climatedataguide.ucar.edu/climate-data/hurrell-north-atlantic-oscillation-nao-index-pc-based`)

Jayne, S. R., & Marotzke, J. (2002). The Oceanic Eddy Heat Transport. *Journal of Physical Oceanography*, *32*(12), 3328-3345. doi: 10.1175/1520-0485(2002)032<3328:TOEHT>2.0.CO;2

Jones, H., & Marshall, J. (1997). Restratification after Deep Convection. *Journal of Physical Oceanography*, *27*(10), 2276-2287. doi: 10.1175/1520-0485(1997)027<2276:RADC>2.0.CO;2

Kawasaki, T., & Hasumi, H. (2014). Effect of freshwater from the West Greenland Current on the winter deep convection in the Labrador Sea. *Ocean Modelling*, *75*, 51 - 64. doi: https://doi.org/10.1016/j.ocemod.2014.01.003

Laepple, T., & Huybers, P. (2014). Ocean surface temperature variability: Large model–data differences at decadal and longer periods. *Proceedings of the National Academy of Sciences*, *111*(47), 16682–16687. doi: 10.1073/pnas.1412077111

Large, W. G., McWilliams, J. C., & Doney, S. C. (1994). Oceanic vertical mixing: A review and a model with a nonlocal boundary layer parameterization. *Review of Geophysics*, *32*(4), 363-403. doi: 10.1029/94RG01872

Large, W. G., & Yeager, S. G. (2009). The global climatology of an interannually varying air–sea flux data set. *Journal of Climate*, *33*(341). doi: 10.1007/s00382-008-0441-3

Lavender, K. L., Davis, R. E., & Owens, W. B. (2002). Observations of Open-Ocean Deep Convection in the Labrador Sea from Subsurface Floats. *Journal of Physical Oceanography*, *32*(2), 511-526. doi: 10.1175/1520-0485(2002)032<0511:OOOODC>2.0.CO;2

Lilly, J. M., Rhines, P. B., Schott, F., Lavender, K., Lazier, J. R. N., & Send, U. (2003). Observations of the Labrador Sea Eddy Field. *Process in Oceanography*, *59*(1), 75–176.

Lohmann, G., Butzin, M., Eissner, N., Shi, X., & Stepanek, C. (2020). Abrupt Climate and Weather Changes Across Time Scales. *Paleoceanography and Paleoclimatology*, *35*(9). doi: 10.1029/2019pa003782

Lohmann, G., Pfeiffer, M., Laepple, T., Leduc, G., & Kim, J.-H. (2013). A model–

data comparison of the Holocene global sea surface temperature evolution. *Climate of the Past*, *9*(4), 1807–1839. doi: 10.5194/cp-9-1807-2013

Lorenz, E. N. (1955). Available Potential Energy and the Maintenance of the General Circulation. *Tellus*, *7*(2), 157-167. doi: 10.1111/j.2153-3490.1955.tb01148.x

Marchesiello, P., McWilliams, J. C., & Shchepetkin, A. (2003). Equilibrium Structure and Dynamics of the California Current System. *Journal of Physical Oceanography*, *33*(4), 753-783. doi: 10.1175/1520-0485(2003)33<753:ESADOT>2.0.CO;2

Marshall, J., & Schott, F. (1999). Open-ocean convection: Observations, theory, and models. *Review of Geophysics*, *37*(1), 1–64.

Marshall, J., & Shutts, G. (1981). A Note on Rotational and Divergent Eddy Fluxes. *Journal of Physical Oceanography*, *11*(12), 1677-1680. doi: 10.1175/1520-0485(1981)011<1677:ANORAD>2.0.CO;2

McGeehan, T., & Maslowski, W. (2011). Impact of Shelf–Basin Freshwater Transport on Deep Convection in the Western Labrador Sea. *Journal of Physical Oceanography*, *41*(11), 2187-2210. doi: 10.1175/JPO-D-11-01.1

Olbers, D., Willebrand, J., & Eden, C. (2012). *Ocean Dynamics*. Springer, Berlin, Heidelberg. doi: https://doi.org/10.1007/978-3-642-23450-7

Palter, J. B., Lozier, M. S., & Lavender, K. L. (2008). How Does Labrador Sea Water Enter the Deep Western Boundary Current? *Journal of Physical Oceanography*, *38*(5), 968-983. doi: 10.1175/2007JPO3807.1

Redi, M. H. (1982). Oceanic Isopycnal Mixing by Coordinate Rotation. *Journal of Physical Oceanography*, *12*(10), 1154-1158. doi: 10.1175/1520-0485(1982)012<1154:OIMBCR>2.0.CO;2

Renault, L., Molemaker, M. J., McWilliams, J. C., Shchepetkin, A. F., Lemarié, F., Chelton, D., … Hall, A. (2016). Modulation of Wind Work by Oceanic Current Interaction with the Atmosphere. *Journal of Physical Oceanography*, *46*(6), 1685-1704. doi: 10.1175/JPO-D-15-0232.1

Rhein, M., Kieke, D., & Steinfeldt, R. (2015). Advection of North Atlantic Deep Water from the Labrador Sea to the southern hemisphere. *Journal of Geophysical Research: Oceans*, *120*(4), 2471–2487. doi: 10.1002/2014JC010605

Rieck, J. K., Böning, C. W., & Getzlaff, K. (2019). The Nature of Eddy Kinetic

Energy in the Labrador Sea: Different Types of Mesoscale Eddies, Their Temporal Variability, and Impact on Deep Convection. *Journal of Physical Oceanography*, *49*(8), 2075-2094. doi: 10.1175/JPO-D-18-0243.1

Rykova, T., Straneo, F., & Bower, A. S. (2015). Seasonal and interannual variability of the West Greenland Current System in the Labrador Sea in 1993–2008. *Journal of Geophysical Research: Oceans*, *120*(2), 1318-1332. doi: 10.1002/2014JC010386

Rykova, T., Straneo, F., Lilly, J. M., & Yashayaev, I. (2009). Irminger Current Anticyclones in the Labrador Sea observed in the hydrographic record, 1990–2004. *Journal of Marine Research*, *67*(3), 361-384. doi: doi:10.1357/002224009789954739

Saenko, O. A., Dupont, F., Yang, D., Myers, P. G., Yashayaev, I., & Smith, G. C. (2014). Role of Resolved and Parameterized Eddies in the Labrador Sea Balance of Heat and Buoyancy. *Journal of Physical Oceanography*, *44*(12), 3008–3032. doi: 10.1175/JPO-D-14-0041.1

Schmidt, S., & Send, U. (2007). Origin and Composition of Seasonal Labrador Sea Freshwater. *Journal of Physical Oceanography*, *37*(6), 1445–1454. doi: 10.1175/jpo3065.1

Sidorenko, D., Goessling, H., Koldunov, N., Scholz, P., Danilov, S., Barbi, D., … Jung, T. (2019). Evaluation of FESOM2.0 Coupled to ECHAM6.3: Preindustrial and HighResMIP Simulations. *Journal of Advances in Modeling Earth Systems*, *11*(11), 3794-3815. doi: https://doi.org/10.1029/2019MS001696

Soufflet, Y., Marchesiello, P., Lemarié, F., Jouanno, J., Capet, X., Debreu, L., & Benshila, R. (2016). On effective resolution in ocean models. *Ocean Modelling*, *98*, 36–50. doi: 10.1016/j.ocemod.2015.12.004

Straneo, F. (2006). Heat and Freshwater Transport through the Central Labrador Sea. *Journal of Physical Oceanography*, *36*(4), 606–628.

Vallis, G. K. (2017). *Atmospheric and Oceanic Fluid Dynamics – Fundamentals and Large-Scale Circulation* (2nd ed.). Cambridge University Press.

von Storch, J.-S., Eden, C., Fast, I., Haak, H., Hernández-Deckers, D., Maier-Reimer, E., … Stammer, D. (2012). An Estimate of the Lorenz Energy Cycle for the World Ocean Based on the STORM/NCEP Simulation. *Journal of Physical Oceanography*, *42*(12), 2185-2205. doi: 10.1175/JPO-D-12-079.1

Wang, Q., Danilov, S., Sidorenko, D., Timmermann, R., Wekerle, C., Wang, X., … Schröter, J. (2014). The Finite Element Sea Ice-Ocean Model (FESOM) v.1.4: formulation of an ocean general circulation model. *Geoscientific Model Development*, *7*(2), 663-693. doi: 10.5194/gmd-7-663-2014

Yashayaev, I., & Loder, J. W. (2016). Recurrent replenishment of Labrador Sea Water and associated decadal-scale variability. *Journal of Geophysical Research: Oceans*, *121*(11), 8095-8114. doi: 10.1002/2016JC012046

Zdunkowski, W., & Bott, A. (2003). The Helmholtz theorem. In *Dynamics of the Atmosphere: A Course in Theoretical Meteorology* (p. 214–217). Cambridge University Press. doi: 10.1017/CBO9780511805462.014

Zhang, W., & Yan, X.-H. (2014). Lateral Heat Exchange after the Labrador Sea Deep Convection in 2008. *Journal of Physical Oceanography*, *44*(12), 2991-3007. doi: 10.1175/JPO-D-13-0198.1

Zhang, W., & Yan, X.-H. (2018). Variability of the Labrador Sea Surface Eddy Kinetic Energy Observed by Altimeter From 1993 to 2012. *Journal of Geophysical Research: Oceans*, *123*(1), 601-612. doi: 10.1002/2017JC013508

Zhang, Z., Wang, W., & Qiu, B. (2014). Oceanic mass transport by mesoscale eddies. *Science*, *345*(6194), 322–324. doi: 10.1126/science.1252418

References From the Supporting Information

Amante, C., & Eakins, B. W. (2009). *ETOPO1 1 Arc-Minute Global Relief Model: Procedures, Data Sources and Analysis* (NOAA Technical Memorandum NESDIS No. NGDC-24). NOAA. ([July 15 2015]) doi: 10.7289/V5C8276M

Griffies, S. M., Danabasoglu, G., Durack, P. J., Adcroft, A. J., Balaji, V., Böning, C. W., … Yeager, S. G. (2016). OMIP contribution to CMIP6: experimental and diagnostic protocol for the physical component of the Ocean Model Intercomparison Project. *Geoscientific Model Development*, *9*(9), 3231–3296. doi: 10.5194/gmd-9-3231-2016

Griffies, S. M., Winton, M., Samuels, B., Danabasoglu, G., Yeager, S. G., Marsland, S. J., … Bentsen, M. (2012). *Datasets and protocol for the CLIVAR WGOMD Coordinated Ocean-sea ice Reference Experiments (COREs)* (WCRP Report No. No. 21/2012).

Kelley, D., & Richards, C. (2021). oce: Analysis of Oceanographic Data [Computer software manual]. Retrieved from `https://CRAN.R-project.org/package=oce` (R package version 1.4-0)

Locarnini, R. A., Mishonov, A. V., Antonov, J. I., Boyer, T. P., Garcia, H. E., Baranova, O. K., … Seidov, D. (2013). *World Ocean Atlas 2013, Volume 1: Temperature. S. Levitus.* Ed., A. Mishonov technical editor, NOAA Atlas NESDIS 73.

Scholz, P., Kieke, D., Lohmann, G., Ionita, M., & Rhein, M. (2014). Evaluation of Labrador Sea Water formation in a global Finite-Element Sea-Ice Ocean Model setup, based on a comparison with observational data. *Journal of Geophysical Research: Oceans*, *119*(3), 1644-1667. doi: 10.1002/2013JC009232

Steele, M., Morley, R., & Ermold, W. (2001). PHC: A Global Ocean Hydrography with a High-Quality Arctic Ocean. *Journal of Climate*, *14*(9), 2079-2087. doi: 10.1175/1520-0442(2001)014<2079:PAGOHW>2.0.CO;2

Wekerle, C., Wang, Q., von Appen, W.-J., Danilov, S., Schourup-Kristensen, V., & Jung, T. (2017). Eddy-Resolving Simulation of the Atlantic Water Circulation in the Fram Strait With Focus on the Seasonal Cycle. *Journal of Geophysical Research: Oceans*, *122*(11), 8385-8405. doi: 10.1002/2017JC012974